ROYAL SOCIETY
OF CHEMISTRY

PAPER

Check for updates

Structure–property relationship in phenothiazine-based hypercrosslinked organic electrode materials through porosity adjustment

Hakan Bildirir, †[ab] Nagaraj Patil, †[a] Sergio Pinilla,[a] Marta Liras *[b] and Rebeca Marcilla *[a]

A series of phenothiazine-based hypercrosslinked p-type porous polymers were synthesized *via* a knitting polymerization method, incorporating increasing amounts of benzene as a co-monomer for a systematic observation of the porosity–electrochemical performance relationship. The resulting materials, denoted as IEP-29, IEP-29-b/4, IEP-29-b/2, and IEP-29-b, correspond to PTz/benzene ratios of 1/0, 1/0.25, 1/0.5, and 1/1, respectively. The inclusion of benzene, acting as a structure directing co-monomer, significantly increased the crosslinking density and accessible surface areas, which varied from 29 $m^2\ g^{-1}$ (IEP-29, no benzene) to 586 $m^2\ g^{-1}$ (IEP-29-b, 1/1 ratio). However, this also resulted in reduced theoretical capacity, which decreased from 112 $mA\ h\ g^{-1}$ (IEP-29) to 70 $mA\ h\ g^{-1}$ (IEP-29-b), due to the incorporation of non-electrochemically active benzene units. Electrochemical testing in Li-cells revealed that increased crosslinking improved capacity utilization and high-rate capability, despite a moderate decline in gravimetric capacity. This study further explored the effect of increasing electrode mass loading (up to 50 $mg\ cm^{-2}$) on electrochemical performance. Remarkably, IEP-29-b, the most crosslinked analogue, exhibited near-linear areal capacity scaling with minimal loss in gravimetric capacity as mass loading increased. At 50 $mg\ cm^{-2}$, it achieved 3.5 $mA\ h\ cm^{-2}$ along with excellent rate performance and cycling stability, retaining 71% of its capacity after 500 cycles at 2C. Importantly, the moderately crosslinked analogue (IEP-29-b/4) offered an optimal balance between specific gravimetric and areal capacities, delivering record-high values of 72.9 $mA\ h\ g^{-1}$ (based on the total mass of the electrode) and 3.85 $mA\ h\ cm^{-2}$, respectively – among the highest reported for p-type polymer cathodes in lithium cells. This work presents a cost-effective, scalable route to develop crosslinked, porous p-type hyperbranched polymers as high-performance cathodes with enhanced electrochemical properties at both the material and electrode levels. Therefore, this strategy paves the way for more commercially viable, high-capacity energy storage solutions.

1. Introduction

The shift toward sustainable energy is driven by the finite nature of fossil fuels and the urgent need to reduce CO_2 emissions contributing to climate change.[1] The deployment of renewable energy sources – such as wind and sun power – alongside the electrification of transport, is at the forefront of this transition.[2] Batteries play a pivotal role in this energy transition as they help to mitigate the mismatch between energy demand/generation inherent in intermittent renewable sources, and they are essential components in electrical vehicles.[2–4] However, the growing demand for high-performance batteries has significantly increased the consumption of key raw materials.[5] This trend raises concerns regarding supply chain risk and the long-term sustainability of commercial battery technologies, which rely on inorganic electrodes containing critical raw materials.[6]

In this context, organic electrode materials (OEMs) offer a promising alternative since they can be produced from abundant and globally available starting materials.[7–9] However, early OEMs, mainly conducting polymers like polyaniline and polythiophene, showed limited electrochemical performance, with low theoretical capacities due to inefficient charge stabilization (*e.g.* at least 3 thiophene units are needed to delocalize one electron during oxidation).[10] Additional issues such as self-discharge further hindered their development.[11] Recent advances have renewed interest in OEMs through the integration of redox-active groups, where charge transfer occurs at localized molecular sites rather than along extended conjugation, enhancing capacity, reversibility, and stability.[12]

[a]Electrochemical Processes Unit, IMDEA Energy, Avda. Ramón de la Sagra 3, Móstoles, Madrid, 28935, Spain. E-mail: rebeca.marcilla@imdea.org

[b]Photoactivated Processes Unit, IMDEA Energy, Avda. Ramón de la Sagra 3, Móstoles, Madrid, 28935, Spain. E-mail: marta.liras@imdea.org

† These authors contributed equally.

35242 | *J. Mater. Chem. A*, 2025, **13**, 35242–35256

This journal is © The Royal Society of Chemistry 2025

Organic electrode materials (OEMs) are primarily classified as n-type or p-type based on their redox behavior. n-type materials, more extensively studied, contain electron-withdrawing groups such as carbonyls (e.g., naphthalene diimide (NDI) and anthraquinone) or sp^2-hybridized nitrogen atoms (e.g., phenazine),[13,14] and tend to be reduced via the acceptance of one electron. p-type materials, by contrast, involve oxidation through the donation of unpaired electrons at heteroatoms (e.g., sulfur in thianthrene and nitrogen in phenothiazine),[15] with nitroxyl-based polymers like poly(4-methacryloyloxy-2,2,6,6-tetramethylpiperidine-1-oxyl) (PTMA) being widely used as cathodes.[16]

Despite their promise, the two major drawbacks associated with organic electrode materials (OEMs) are their inherently low electrical conductivity and high solubility—particularly in the case of small redox-active molecules.[17] Mixing OEMs with conductive carbon additives (conventional carbon content: 40–50%) has been found to be a successful approach to overcome the limitations posed by low conductivity. Furthermore, the high solubility of small molecules can be mitigated by forming their macromolecular analogues (i.e. their polymers), which offer improved stability and reduced solubility in the electrolyte.[12,18] Ultimately, immobilization of these compounds along (hyper)crosslinked or porous polymeric frameworks offers superior stability, as crosslinking reduces solubility and improves (hydro)thermal stability.[19–22]

It is widely recognized that achieving areal capacities exceeding 3 mA h cm^{-2} is a critical requirement for the practical deployment of lithium-ion batteries, particularly in high-energy applications such as grid-scale storage and electric vehicles.[23,24] However, a persistent limitation of OEMs, whether small molecules or polymers, is their typically low-to-moderate values of areal capacities (mAh cm^{-2}). Although increasing the mass loading of the active material (mg cm^{-2}) appears to be a straightforward approach to enhance areal capacity, it often results in a significant decline in performance, mainly associated with intrinsic limitations in electron and ion transport within thick electrodes.[25,26] This limited electrochemical performance includes underutilization of active materials, diminished rate capability, stability issues, and manufacturing complexities.[27] In this regard, porous organic electrodes are promising alternatives to non-porous OEMs, due to their permanently porous skeleton, which provides enhanced accessibility of the electrolyte to redox-active moieties.[22] This inherent porosity facilitates charge transport across the entire electro thickness,[28] hence enhancing kinetics and maximizing material utilization.

Phenothiazine (PTz) is a widely used building block in the design of porous materials with diverse applications ranging from gas separation to photocatalysis.[29–32] In recent years, the redox-active nature of PTz and its derivatives has also been exploited in the design of porous and hypercrosslinked OEMs for electrochemical energy storage.[33–37] Building on this, our group previously developed a PTz-based hypercrosslinked polymer, IEP-29, which demonstrated promising electrochemical performance as a Li-ion battery cathode.[38] However, due to the linear geometry of the PTz monomer, pore formation was constrained, leading to a material with very low accessible surface area ($S_{BET} < 30$ m^2 g^{-1}). Despite its limited porosity, IEP-29 demonstrated very good electrochemical performance, particularly at moderate mass loadings (~2 mg cm^{-2}).[38] These encouraging results prompted further investigation into whether promoting material porosity could yield additional performance gains.

Here, we present the co-polymerization of PTz with benzene as a co-monomer, which acts as a pore-structuring agent, to systematically explore the structure–property relationship between porosity and electrochemical performance. Although the addition of the redox-inactive benzene co-monomer inherently reduced the theoretical capacities, it simultaneously introduced a higher degree of crosslinking and enhanced porosity. These structural features significantly improved some key electrochemical properties such as capacity utilization, intrinsic kinetics, rate performance, and cycling stability. Importantly, this study prioritizes practical electrode configurations, including high polymer content and mass loading, deliberately normalizing key performance indicators with respect to electrode area and total mass, which are more relevant for real-world applications (high polymer content and high mass loading).
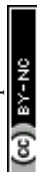
2. Experimental details

2.1. Materials and instruments

10-Methyl-10H-phenothiazine (PTz, 98%), formaldehyde dimethyl acetal (FDA, 98%) and FeCl$_3$ (98%) were received from Alfa Aesar whereas anhydrous 1,2-dichloroethane (DCE, 99.5%, AcroSeal) was bought from Acros Chemicals (Thermo Scientific Chemicals). Ethylene carbonate (EC), N-methyl-2-pyrrolidone (NMP), isopropyl alcohol (IPA), methanol (MeOH), tetrahydrofuran (THF), and chloroform (CHCl$_3$) used for electrode preparation and work-up (washing, Soxhlet extraction, etc.) were bought from Sigma-Aldrich and were of HPLC grade. Additionally, lithium foil (600 μm), and Celgard (2500) were also received from Sigma-Aldrich. Nanografi was chosen to purchase reduced graphene oxide (RGO) and single-walled carbon nanotubes (SWCNTs). The electrolyte solution, 1 M LiPF$_6$ in EC/DCM (1/1, v/v), was a product of Solvionic, and used as received.

A Micromeritics Tristar II Plus was used for gas sorption measurements. ATR-IR was conducted using a Thermo Fisher Scientific Nicolet 6700. A Bruker AVIII/HD spectrometer and Bruker Ultrashield 500 Plus console Advance III were used to measure solid-state CP-MAS ^{13}C NMR (100 MHz) and solution ^{13}C NMR (125 MHz) spectra, respectively. CHNS elemental analyses were conducted via a Thermo Flash Smart. A Netzsch STA 449 F3 Jupiter was used to conduct thermal gravimetric analysis (TGA) and the ramp rate was 5 °C min^{-1} until 900 °C either under argon or air. A JEOL JSM-7900F was used for capturing high-resolution scanning electron microscopy (SEM) images.

2.2. Syntheses of IEP-29 analogues

IEP-29 was prepared using the previously published procedure, yielding 83%.[38] The co-polymers were synthesized using

This journal is © The Royal Society of Chemistry 2025

J. Mater. Chem. A, 2025, **13**, 35242–35256 | **35243**

a slightly modified method. As an example, synthesis of IEP-29-b/4 (Table S1): 1.80 g FeCl₃ and 0.5 g PTz were placed in a 100 mL three-neck flask and 25 mL one-neck flask in a glovebox, respectively, and sealed. The three-neck flask was connected to a condenser under Ar flow. 13 mL and 5 mL anhydrous DCE was added to three-neck and one-neck flasks, respectively. Stirring of the mixture in the three-neck flask was started to obtain a good dispersion of FeCl₃. Following this, 0.05 mL benzene and 0.98 mL FDA were added to the one-neck flask, and the total mixture in the one-neck flask was slowly added to the FeCl₃ dispersion under Ar. The color rapidly changed to dark red, and some solid was formed in a few hours. After an overnight reaction (approx. 18 hours), the reaction was cooled down to room temperature, and quenched with 5 mL of MeOH. Then, the solid was collected by vacuum filtration, and washed with 100 mL MeOH, 100 mL THF, 100 mL water, 20 mL MeOH (to remove the water), and 100 mL CHCl₃. Following this, the solid was placed in a Soxhlet extractor and washed intensively with MeOH. The solid was dried under vacuum at 60 °C, and yielded 88%. IEP-29-b/2 and IEP-29-b were prepared using the same procedure, with the respective equivalent amounts of reactants, and yields are detailed in Tables S2 and S3, respectively.

2.3. Preparation of buckypaper electrodes

We fabricated self-supporting IEP-29 series buckypaper electrodes without binders or metal current collectors using a modified version of our previous method.[39] To evaluate the impact of composition, we prepared electrodes with polymer contents ranging from 50 to 90 wt% while keeping the polymer mass loading constant at 2.0 mg cm⁻². Additionally, we explored the feasibility of polymer-based electrodes by preparing IEP-29, IEP-29-b/4, and IEP-29-b variants with a fixed 90/10 wt% polymer-to-carbon additive ratio and mass loadings between 2.5 and 50 mg cm⁻². As an example, a buckypaper electrode with a 60 : 20 : 20 wt% composition (IEP-29 : SWCNTs : rGO) and a polymer mass loading of ~2.5 mg cm⁻² was prepared as follows:

First, 13.3 mg of SWCNTs were dispersed in 20 mL of isopropanol (IPA) using a tip sonicator (UP400S, 400 W, 24 kHz) for 10 minutes for 0.75 cycles at full amplitude. Next, we ground 13.3 mg of rGO with 40 mg of IEP-29, and added this mixture to

the SWCNT dispersion. The solution underwent bath sonication (Branson 2510, 100 W, 42 kHz) for 2 hours, followed by continuous stirring overnight to create a uniform electrode ink. The ink was then vacuum-filtered through a 47 mm nylon membrane (0.45 μm pore size) to form buckypaper. After carefully peeling it from the filter, we dried it overnight at 70 °C under vacuum. Finally, we cut the material into 12 mm circular discs, which were ready for use as electrodes.

2.4. Assembly of coin cells

We assembled CR2032 coin-type Li-cells using a porous Whatman® glass microfiber filter (Grade GF/B) saturated with 150 μL of electrolyte, consisting of 1 M LiPF₆ dissolved in a 1 : 1 mixture of ethylene carbonate (EC) and diethyl carbonate (DEC). The IEP-29 series buckypaper acted as the working electrode, while lithium foil served as both the counter and reference electrode. To ensure a contamination-free environment, all cell assembly took place inside a high-purity argon-filled glovebox (MBraun) with moisture and oxygen levels maintained below 0.5 ppm and 1.5 ppm, respectively.

Further materials, instruments and experimental details for electrochemical characterization can be found in the SI.

3. Results and discussion

3.1. Syntheses and characterization of IEP-29 polymer analogues

The knitting method *via* Friedel–Crafts alkylation is a frequently applied technique for the syntheses of hypercrosslinked and porous polymers for various applications.[40] The method is particularly interesting since it allows facile tuning of the functionality and porosity *via* addition of a variety of aromatic monomers and formaldehyde dimethyl acetal (FDA) as the crosslinking agent.[41–45] Therefore, knitting polymerization was chosen as a suitable and facile method to tune the porous properties of the series of PTz-based hypercrosslinked polymers (Scheme 1).

Among these, IEP-29 is assumed to be the homopolymer of PTz, as the contribution of the formaldehyde dimethyl acetal (FDA) cross-linking agent is considered negligible. Further crosslinked analogues were synthesized following the same synthetic route, *via* adding different equivalents of benzene
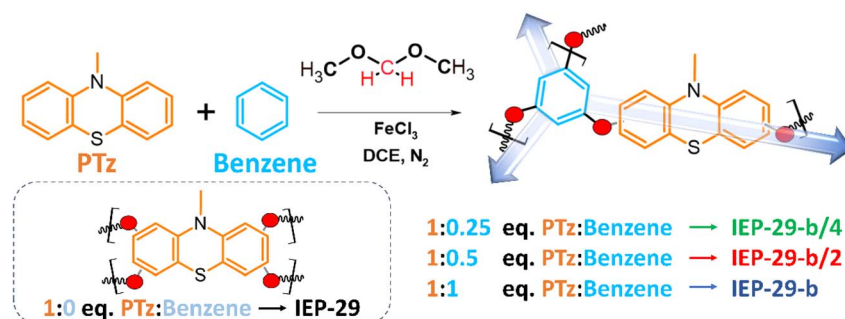
Scheme 1 Schematic illustration of the syntheses of the IEP-29 series. Red circles represent methylene bridges coming from the FDA cross-linking agent while arrows represent the contribution of benzene as the structure directing co-monomer.

35244 | *J. Mater. Chem. A*, 2025, **13**, 35242–35256

This journal is © The Royal Society of Chemistry 2025

(0.25, 0.5, and 1 equivalents *vs.* PTz) as the co-monomer and porosity promoter. These were denoted according to their monomer ratios: IEP-29-b/4 (0.25 eq.), IEP-29-b/2 (0.5 eq.), and IEP-29-b (1 eq.), respectively (see Experimental details and Tables S1–S3 in the SI for further information). Notably, each benzene ring contains six reactive positions that can participate in the crosslinking reaction with formaldehyde dimethyl acetal (FDA), making benzene an excellent structure-directing unit capable of promoting extensive network formation through dense and uniform crosslinking. Even though solid hyperbranched polymer particles were quickly formed in all four cases, significant macroscopic differences were observed in the course of the reactions. Briefly, the reaction mixture solidified (*i.e.* only a solid crude mixture was visible from outside the flask) in almost 30 min in the case of IEP-29-b, whereas a similar situation occurred for IEP-29-b/2 after 2 hours. On the other hand, the reaction mixture of both IEP-29-b/4 and IEP-29 became a highly viscous dispersion of polymeric particles after a few hours, and stayed the same until the end of the corresponding reactions.

Since the main aim of adding benzene was to enhance accessible surface areas along the polymer backbone through higher crosslinking and reduced flexibility,[46] nitrogen physisorption measurements were conducted. Remarkably, significantly higher Brunauer, Emmett and Teller (BET) surface areas (S_{BET}) were observed for the analogues having more benzene as the co-monomer (see Fig. 1b and 2b). Specifically, on just

adding 0.25 eq. of benzene (IEP-29-b/4) S_{BET} increased from 29 to 254 m^2 g^{-1}. Moreover, doubling the benzene equivalent to reach a 2 : 1 PTz : benzene ratio (IEP29-b/2) resulted in slightly more than double the value (559 m^2 g^{-1}). However, the S_{BET} did not linearly improve from the half equivalent to the equimolar ratio (1PTz : benzene), and the S_{BET} for IEP-29-b was just barely higher (586 m^2 g^{-1}) than that of IEP-29-b/2. This non-linear trend is probably due to the rapid solidification of their reaction mixtures as a consequence of very high crosslinking as stated above. Such early solidification may hinder extended micropore formation by bypassing the intermediate "gelation" stage proposed in polymer porosity formation models,[47] and hence the possibility of the lack of efficient crosslinking for further amounts of benzene. This hypothesis is supported by the shape of the isotherms of IEP-29-b/2 and IEP-29-b, which show nearly the same uptake at low-relative pressures (P/P_0), indicating comparable microporosity (Fig. 1b). On the other hand, the steep increase at high relative pressures and slight hysteresis in the case of IEP-29-b indicates similar type II and IV isotherms,[48] which means additional adsorption on the external surface or within the mesopores, a behavior consistent with previously reported benzene homopolymers[49,50] and benzene-rich co-polymers synthesized *via* the knitting method.[42] Although pore size distributions derived from density functional theory (DFT) may not provide highly accurate results for amorphous porous polymers,[51] the calculations performed on the porous IEP-29 analogues yielded values consistent with
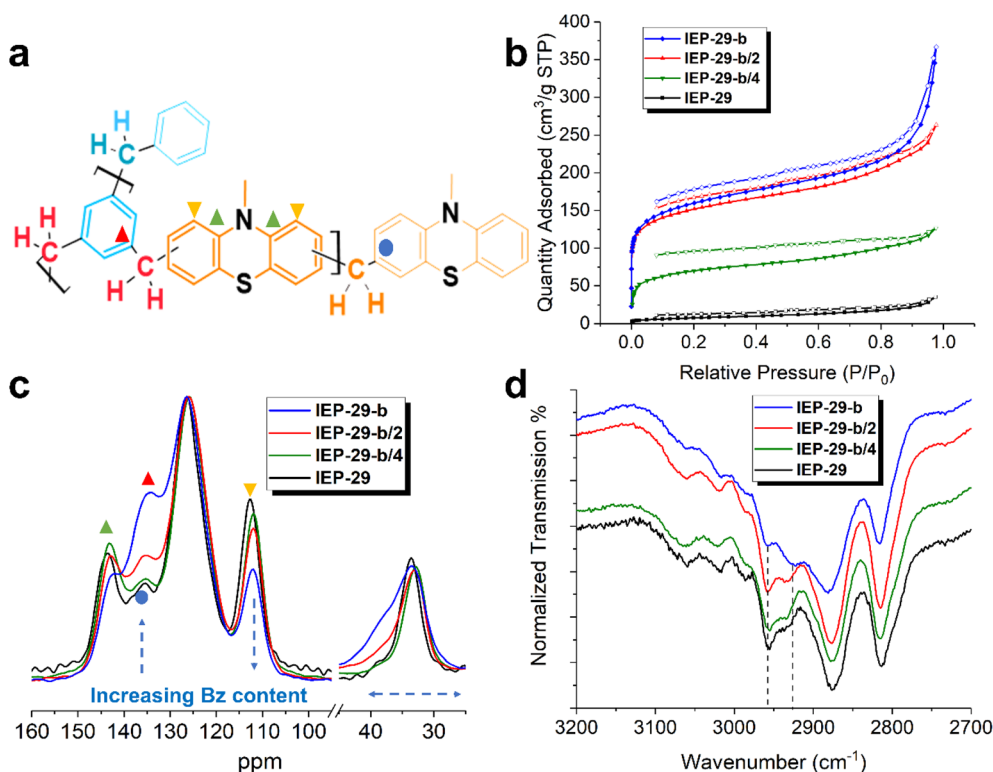

Fig. 1 (a) Prediction of possible structural forms along the polymeric backbones and proposed peak locations of some carbons in ^{13}C NMR in (c). (b) Gas sorption isotherms of IEP-29, IEP-29-b/4, IEP-29-b/2, and IEP-29-b. (c) Solid-state ^{13}C NMR spectra of IEP-29, IEP-29-b/4, IEP-29-b/2, and IEP-29-b. (d) FT-IR spectra of IEP-29, IEP-29-b/4, IEP-29-b/2, and IEP-29-b.
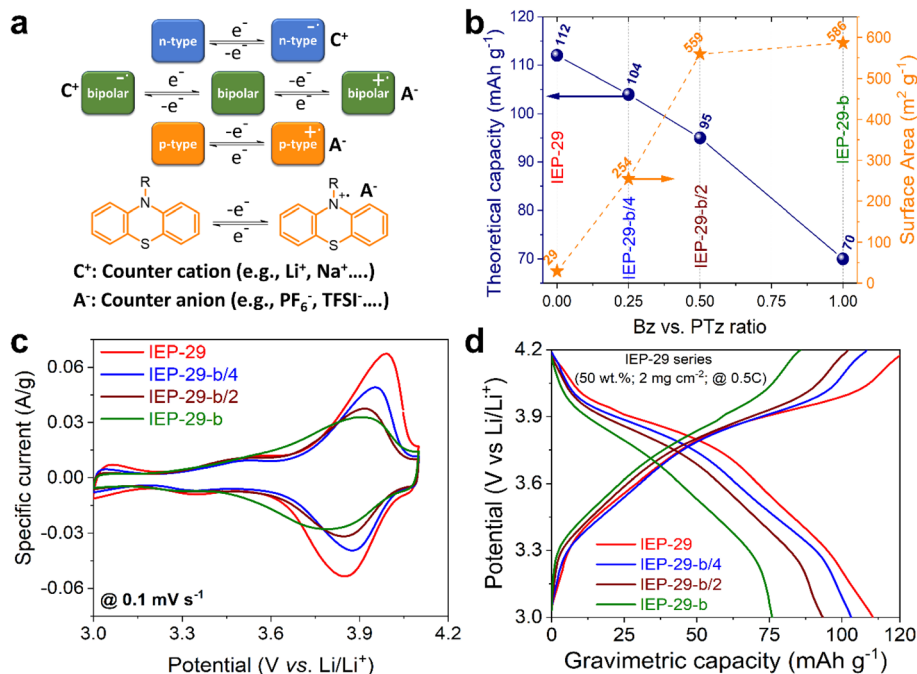
Fig. 2 (a) Schematic representation of general redox mechanisms of OEMs (A^- is PF_6^- in this work). (b) Prediction of theoretical gravimetric capacity and BET surface area of the IEP-29 series with different benzene-to-PTz ratios. (c) Representative CVs and GCDs (d) of IEP-29, IEP-29-b/4, IEP-29-b/2, and IEP-29-b in Li-cells at 0.1 mV s^{-1} and 0.5C, respectively. The polymer content and mass loading are 50 wt% and 2 mg cm^{-2}, respectively.

those typically observed for hypercrosslinked polymers (Fig. S1).[51,52]

[13]C solid-state Cross-Polarization Magic-Angle-Spinning (CP-MAS) NMR studies indicated the successful incorporation of all monomeric units as expected (Fig. 1a, c and S2a). Higher amounts of benzene as the co-monomer resulted in an obvious increase and reduction of the relative peak intensities of aromatic carbons at 135 ppm and 113 ppm, respectively. The former peak can be attributed to the aromatic carbons neighboring the methylene bridges ($-CH_2-$) whereas the latter should be from the highlighted carbon of the PTz unit in Fig. 1b. Additionally, some widening of the aliphatic carbons at around 35 ppm was observed with the higher amounts of benzene, which should be due to extended crosslinking and increased population of mixed $-CH_2-$ bridges along the polymeric backbones. Even though significant differences were not observed in the FT-IR (Fig. 1d) spectra since the IR active groups are identical for all analogues (Fig. S2b), a visible change was observed in the relative intensities of asymmetric C–H stretches[53] along the backbones. Fig. 1d shows that the peak at 2960 cm^{-1}, assigned to the vibrations of the N-methyl ($-N-CH_3$) group of PTz moieties, decreased with increasing benzene content, which resulted in the relative increase of the peak from the methylene bridges ($-CH_2-$) at 2930 cm^{-1}, further confirming the higher degree of crosslinking. Notably, the co-polymerization process involves multiple competing factors—monomer reactivity, size, mobility, and concentration—which collectively complicate a more precise determination of the crosslinking sequence in this randomly "knitted" network.

The broad reflection peaks recorded from the powder X-ray diffraction (pXRD) measurements confirmed that all the formed polymeric materials are amorphous (Fig. S3). Thermal gravimetric analysis (TGA), conducted either under an air or argon atmosphere, showed high thermal stability across all IEP-29 analogues, with no significant differences among the samples (Fig. S4). In contrast, significant textural differences were seen in the high-resolution scanning electron microscopy (HR-SEM) images. Particularly, higher benzene contents led to reduced fibrous morphology and an increase in surface voids (Fig. S5–S8).

The CHNS elemental analysis experiments allowed us to determine the structural composition of the IEP-29 polymer analogues (Table S4). As expected, the percentage of heteroatoms (nitrogen (N) and sulfur (S)), which are exclusively present in the Ptz units decreased with increasing benzene ratio. For example, the sulfur content declined from 3.78 to 2.34 at%, and nitrogen from 3.80 to 2.37 at% across the series from IEP-29 to IEP-29-b, respectively. Despite commonly observed incomplete combustion of such high dimensional polymeric networks,[54,55] the values recorded from the elemental analysis were useful to correlate the theoretical capacity of such random co-polymers. Specifically, the N content was used to estimate the theoretical specific capacities of the co-polymers, considering that the N atom on the PTz moieties is the sole redox-active center (Fig. 2a). According to the % of nitrogen and using IEP-29 as the reference compound (i.e. 100% PTz), with a theoretical gravimetric capacity assumed to be 112 mA h g^{-1}, the estimated theoretical capacities for IEP-29-b/4, IEP-29-b/2,

35246 | J. Mater. Chem. A, 2025, 13, 35242–35256

This journal is © The Royal Society of Chemistry 2025

and IEP-29-b were 104, 95, and 70 mA h g^{-1}, respectively (Fig. 2b and Table S4).

3.2. Electrochemical performance of IEP-29 polymer analogues

Electrochemical characterization of this IEP-29 family was conducted using coin-type Li-cells. Lithium served as both the counter and reference electrode, while 1 M LiPF$_6$ in EC/DEC (1 : 1 by volume) was used as the electrolyte (see the Experimental details in the SI for further information). Self-standing bucky-paper electrodes containing IEP-29 analogues/SWCNTs/rGO were developed, eliminating the need for binders or metal current collectors.[56]

Initially, cyclic voltammetry (CV) was performed on IEP-29 and its further crosslinked derivatives (IEP-29-b/4, IEP-29-b/2, and IEP-29-b) using a buckypaper electrode composed of 50 wt% polymer and 50 wt% carbon additives, with a polymer mass loading of 2 mg cm^{-2}. The CV curves (Fig. 2c) show well-defined redox peaks, characteristic of reversible electrochemical processes involving PF$_6^-$ coordination during oxidation and de-coordination during reduction at the redox-active N site of PTz (see Fig. 2a). Among the tested materials, IEP-29 (red curve) exhibits the highest peak current, indicating superior electro-chemical activity. The oxidation and reduction peaks appear at approximately 3.96 V and 3.87 V, respectively, with a midpoint potential ($E_{1/2}$) around 3.91 V vs. Li/Li$^+$. As the benzyl cross-linking density increases (from IEP-29-b/4 to IEP-29-b), a systematic decrease in peak current is observed, indicating a reduction in the concentration of PTz within the polymer network as expected. The corresponding $E_{1/2}$ values shift slightly, centered at approximately 3.92 V for IEP-29-b, 3.90 V for IEP-29-b/2, and 3.85 V for IEP-29-b/4.

Fig. 2d shows the galvanostatic charge–discharge (GCD) profiles of buckypaper electrodes at a current rate of 0.5C within a potential window of 3.0–4.2 V vs. Li/Li$^+$. The curves feature distinct potential plateaus at around 3.6 V and 3.9 V, charac-teristic of the reversible redox processes in the PTz-based system. The average discharge potential for these materials ranges from 3.66 to 3.68 V (Fig. S9), showing minimal variation and remaining relatively high for organic cathode materials. Among them, IEP-29 achieves the highest gravimetric capacity of approximately 110 mA h g^{-1}. In contrast, the further cross-linked derivatives exhibit progressively lower capacities, with IEP-29-b/4, IEP-29-b/2, and IEP-29-b delivering 103, 94, and 76 mA h g^{-1}, respectively, in line with their theoretical values (Fig. 2a and Table S4).

3.2.1 Optimization of buckypaper electrode composition. The mass loadings of the polymers (i.e., the "active-materials") were set to a standard value (2.0 mg cm^{-2}), and the composition of the buckypaper electrodes was adjusted via varying the polymer content between 50 and 90 wt%. The GCD experiments were carried out at different rates, ranging from 0.5C to 60C, using a coin-type Li-cell configuration. The potential-capacity GCD profiles of these polymers across different C-rates exhibi-ted similar trends, with increased potential polarization at higher rates (Fig. S10–S14). A comparable pattern was observed

in the differential capacity plots at two representative C-rates, 0.5C and 10C (Fig. 3a).

Additionally, coulombic efficiencies were relatively low (87–96%) at ≤1C (Fig. S15) but improved to >98% at rates above 2C, consistent with observations for other phenothiazine-based polymers.[57–59] Fig. 3b presents the gravimetric capacity (based on polymer mass) of the IEP-29 series electrodes with varying compositions across different C-rates, with additional data available in the SI (Fig. S16). At 0.5C, electrodes containing 50, 60, 70, 80, and 90 wt% IEP-29 achieved high gravimetric capacities of 111, 106, 100, 94, and 88 mA h g^{-1}, corresponding to capacity utilizations of 99%, 95%, 90%, 84%, and 78%, respectively (Fig. S17). In contrast, the further cross-linked variants exhibited lower specific capacities, in agreement with their lower calculated theoretical capacities. Specifically, IEP-29-b/4 delivered 102, 98, 92, 86, and 81 mA h g^{-1} while IEP-29-b/2 achieved 94, 93, 87, 81, and 78 mA h g^{-1}. The equimolar version, IEP-29-b, provided 76, 75, 74, 73, and 72 mA h g^{-1} at the same 0.5C rate for 50, 60, 70, 80, and 90 wt% compositions, respec-tively. Interestingly, despite lower specific capacities, the increasing amount of benzene in the polymer structure resulted in better values of capacity utilization that followed the trend: IEP-29-b > IEP-29-b/2 > IEP-29-b/4 > IEP-29. Notably, even at 90 wt% polymer content, IEP-29-b (equimolar Ptz : benzene) maintained nearly 100% capacity utilization – significantly higher than the 78% observed for IEP-29 (no benzene) (Fig. S17).

The rate performance of all these electrodes followed a clear trend: both gravimetric capacity and rate capability declined as the C-rate and polymer content increased (Fig. 3b and c). This effect was particularly significant in electrodes with the highest polymer content (90 wt%) with more limited electronic conductivity, especially at C-rates above 10C. Notably, this capacity decrease with C-rate and polymer content was less evident in polymers with higher surface area (higher benzene ratio) compared to their non-porous analogue IEP-29 (no benzene). For example, at 10C, IEP-29 electrodes with 50, 60, 70, 80, and 90 wt% polymer delivered gravimetric capacities of 75, 70, 55, 56, and 28 mA h g^{-1} (Fig. 3b), corresponding to 70%, 66%, 60%, 54%, and 32% of their respective capacities at 0.5C (Fig. 3c). In contrast, at the same 10C, IEP-29-b (equimolar Ptz : benzene) electrodes with 50, 60, 70, 80, and 90 wt% polymer delivered gravimetric capacities of 59, 53, 49, 45, and 42 mA h g^{-1} (Fig. 3b), corresponding to 75%, 70%, 67%, 62%, and 58% of their respective capacities at 0.5C (Fig. 3c). Overall, capacity retention, and thus rate capability, followed the order IEP-29-b > IEP-29-b/2 > IEP-29-b/4 > IEP-29. Remarkably, even at 90 wt% polymer content, IEP-29-b retained 58% of its capacity (42 mA h g^{-1}), significantly outperforming IEP-29, which retained only 32% (28 mA h g^{-1}). Moreover, after switching the C-rate back to 0.5C following the rate capability test, the cells almost fully regained their original capacity in every case (Fig. S16). This highlights their impressive resilience to high-rate anion storage and shows that capacity degradation remained minimal over 45 cycles.

This stability was confirmed by the long-term cyclability test. Notably, despite containing 90 wt% polymer, the buckypaper
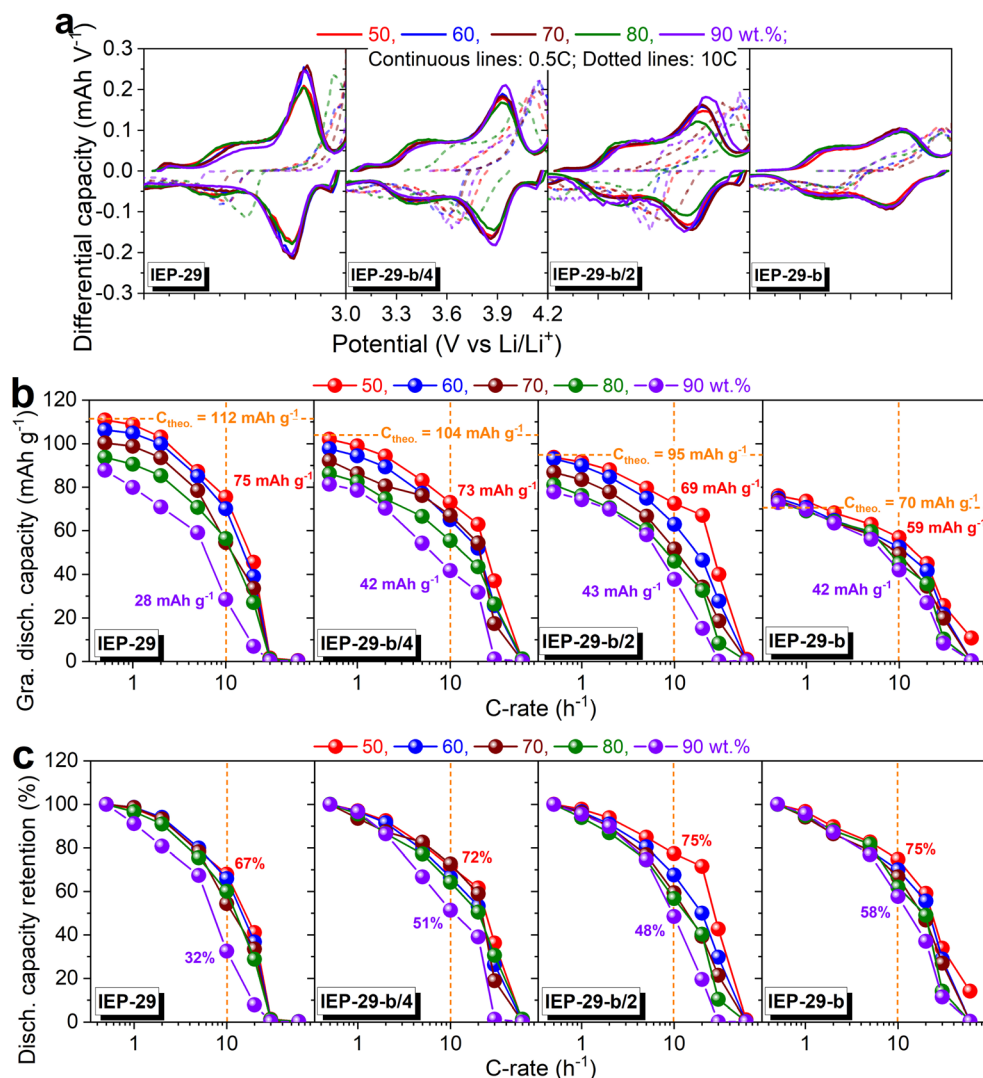
This journal is © The Royal Society of Chemistry 2025

J. Mater. Chem. A, 2025, **13**, 35242–35256 | **35247**

Fig. 3 Rate performance studies of IEP-29 series electrodes (2 mg cm^{-2}) with different polymer/carbon additive ratios in Li-cells: (a) representative differential capacity profiles at 0.5 and 10C. (b) Gravimetric discharge capacity at different C-rates. (c) Discharge capacity retention at different C-rates. The discharge capacities at higher C-rates are normalized with respect to the discharge capacity at 0.5C.

electrodes of IEP-29, IEP-29-b/4, IEP-29-b/2, and IEP-29-b demonstrated durable cycling stability, retaining 69%, 70%, 75%, and 78% capacity after 1000 cycles at 2C, respectively (Fig. S18 and S19). These results evidenced that the long-term stability of the polymer electrodes was enhanced with increasing degrees of crosslinking (higher content of benzene) among the polymer analogues. The enhanced cycling stability of IEP-29-b compared to IEP-29 may stem from structural features introduced by the benzene units. These units likely increase polymer porosity, improving access to redox-active sites and facilitating PF$_6^-$ ion transport. Additionally, the higher degree of crosslinking may reduce solubility in the electrolyte, as suggested by the faster precipitation observed during synthesis. Together, these factors could enhance stability by minimizing active material loss.

3.2.2 Kinetics analysis of IEP-29 series. To uncover why the rate performance increases parallelly with the benzene equivalents (*i.e.* further crosslinking), particularly with a high polymer

loading of 90 wt%, their electrochemical behaviors were closely analyzed. A polymer electrode (2 mg cm^{-2}) with 90 wt% polymer was subjected to a series of tests, including potentiostatic electrochemical impedance spectroscopy (EIS), the galvanostatic intermittent titration technique (GITT), and cyclic voltammetry (CV) across various scan rates (Fig. 4).

EIS was performed at various potentials during both charging and discharging (Fig. S20). All Nyquist plots displayed a depressed semicircle at high frequencies and a sloped line at low frequencies (Fig. 4a and S21), indicative of charge-transfer and diffusion processes. Semicircle fitting results (Fig. S22, details in the SI) revealed that IEP-29 exhibited the highest series resistance (R_S: 11.6–12.2 Ω) and charge-transfer resistance (R_{ct}: 231–359 Ω), suggesting greater bulk resistance and weaker electronic contact. In contrast, the most porous analogue, IEP-29-b, showed the lowest R_S (3.2–6.7 Ω) and R_{ct} (117–286 Ω), indicating enhanced conductivity and interfacial contact. Notably, R_{ct} values were lower at higher states of charge

35248 | *J. Mater. Chem. A*, 2025, **13**, 35242–35256

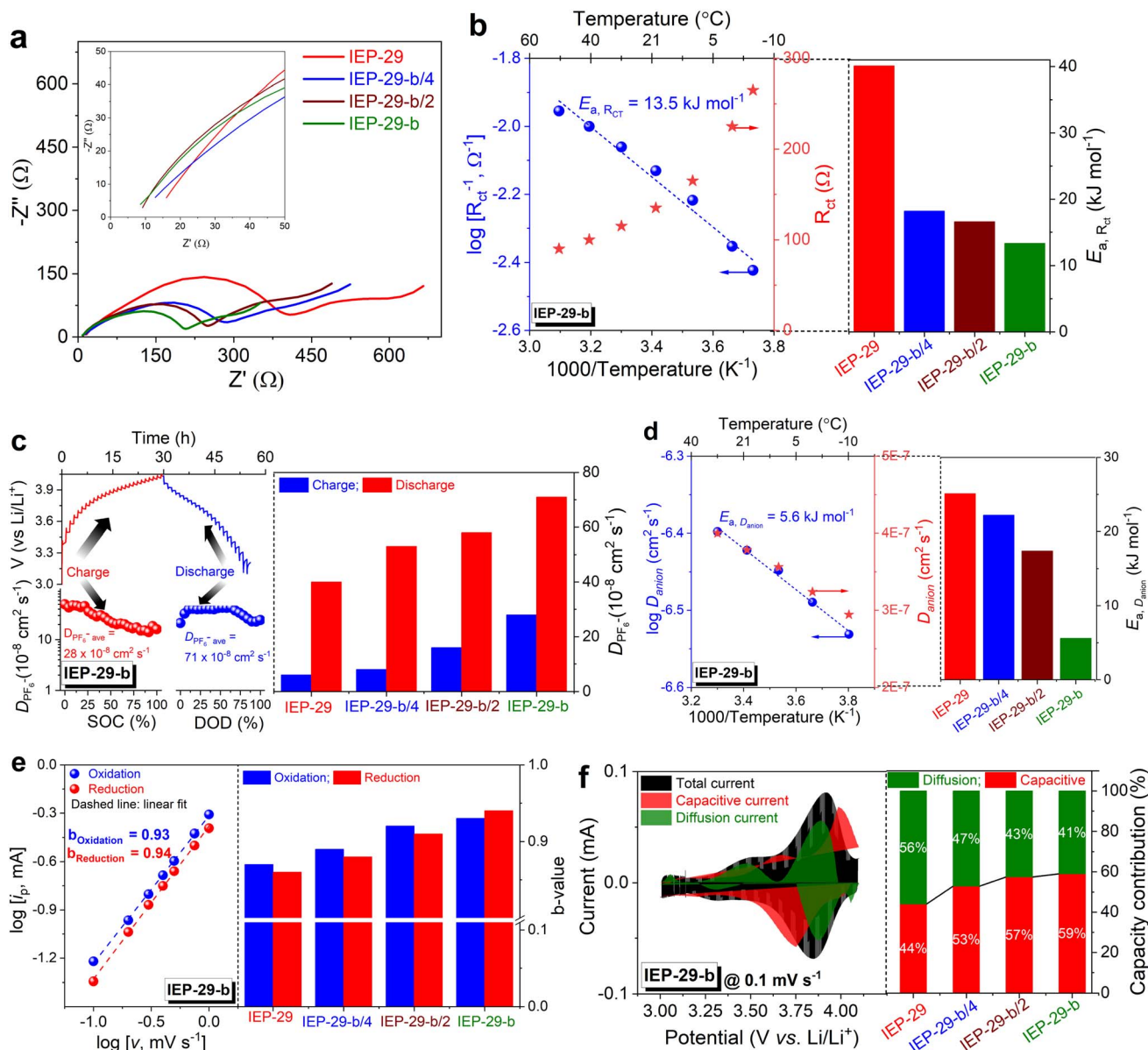This journal is © The Royal Society of Chemistry 2025

Fig. 4 Electrochemical kinetics evaluation of IEP-29 series electrodes in Li-cell: (a) representative Nyquist plots at an equilibrium charging potential of 3.8 V *vs.* Li/Li$^+$. (b) Temperature dependence of R_{ct}, and its fitting with the Arrhenius equation to calculate activation energy, E_a, R_{ct} for the representative IEP-29-b (left). The E_a, R_{ct} for the IEP-29 series is shown on the right. (c) D_{anion} diffusivity as a function of SOC/DOD (bottom range) calculated from GITT measurement (top range) for the representative IEP-29-b (left). The D_{anion} for the IEP-29 series is shown on the right. (d) Temperature dependence of D_{anion}, and its fitting with the Arrhenius equation to calculate activation energy, E_a, D_{anion} for the representative IEP-29-b (left). The E_a, D_{anion} for the IEP-29 series is shown on the right. (e) Peak current *vs.* scan rate on the logarithmic scale to obtain *b*-values according to $i_p = av^b$ for the representative IEP-29-b (left). The *b*-value for the IEP-29 series is shown on the right. Capacitive- and diffusion-controlled current contributions in CV for the representative IEP-29-b at 0.1 mV s^{-1} (left). (f) Capacitive and diffusion contributions calculated by applying the Dunn method for the IEP-29 series at 0.1 mV s^{-1} are shown on the right.

– specifically at 3.8 V (charging), and 4.1 and 3.7 V (discharging) than at lower potentials, likely due to improved ionic mobility and electrode–electrolyte interactions in the charged state. Temperature-dependent EIS (Fig. S24) further supported these observations. Activation energy (E_a, R_{ct}) for charge transfer, calculated from Arrhenius plots ($\log(R_{ct}^{-1})$ *vs.* $1/T$, Fig. 4b and S25), was the lowest for IEP-29-b (13.5 kJ mol^{-1}) and increased progressively with reduced cross-linking, reaching 40.1 kJ mol^{-1}

for IEP-29. This trend highlights faster reaction kinetics in the most highly cross-linked system.

The GITT was used to assess the anion diffusivity (D_{anion}) within the polymer electrode (Fig. 4c and S26, details in the SI). By analyzing the voltage relaxation after each current pulse, D_{anion} values were determined for both charging and discharging processes. IEP-29-b exhibited the highest average diffusivity of 28×10^{-8} cm^2 s^{-1} during charging and 71×10^{-8}

This journal is © The Royal Society of Chemistry 2025

J. Mater. Chem. A, 2025, **13**, 35242–35256 | **35249**

$cm^2 s^{-1}$ during discharging, indicating superior ionic transport. In contrast, IEP-29 showed the lowest values (6×10^{-8} and $40 \times 10^{-8} cm^2 s^{-1}$) while the partially cross-linked variants (IEP-29-b/2 and IEP-29-b/4) displayed intermediate behavior. Temperature-dependent GITT measurements (Fig. S27) showed a consistent trend. The activation energy for anion diffusion (E_a, D_{anion}), derived from Arrhenius plots ($\log(E_a, D_{anion})$ vs. $1/T$; Fig. 4d and S28), was the lowest for IEP-29-b (5.6 kJ mol^{-1}) and increased with decreasing crosslinking density, reaching 25.1 kJ mol^{-1} for IEP-29 (details in the SI). The combined findings achieved from EIS and GITT analysis suggest that higher porosity/crosslinking not only enhances interfacial reaction kinetics but also significantly improves bulk ionic conductivity.

The redox kinetics of the polymer electrodes were further examined using CV at varying scan rates from 0.1 to 1 mV s^{-1} (Fig. S29). Despite the increase in scan rate, the redox peaks retained their symmetrical shape, indicating excellent revers-ibility and fast redox kinetics. To analyze the charge storage mechanism, the peak current (i_p) was plotted against the scan rate (v) on a logarithmic scale, following the power–law rela-tionship $i_p = av^b$ (Fig. 4e and S30, details in the SI).[60] A b-value close to 0.5 suggests diffusion-controlled behavior while a number near 1.0 indicates capacitive dominance. All samples showed high b-values (>0.86), confirming a mixed, or hybrid, charge storage mechanism. Notably, IEP-29-b exhibited the highest capacitive tendency, with b-values of 0.93 (oxidation) and 0.94 (reduction), while IEP-29 showed the lowest (0.87 for oxidation and 0.86 for reduction), reflecting a more diffusion-limited process. To further quantify the contributions of capacitive and diffusion-controlled processes, Dunn's method was applied (Fig. 4f and S31–S34, details in the SI).[61] Even at the lowest scan rate (0.1 mV s^{-1}), IEP-29-b demonstrated a signifi-cant capacitive contribution (59% of the total current), compared to 44% for IEP-29. As the scan rate increased to 1 mV s^{-1}, the capacitive contribution increased accordingly – 82% for IEP-29-b, 81% for IEP-29-b/2, and 78% for IEP-29-b/4, versus 69% for IEP-29 (Fig. S35). This trend is consistent with the scan rate dependence of capacitive processes and correlates well with the high b-values observed.

Overall, the exhaustive analysis of the kinetics revealed that the higher porosity/crosslinking induced in IEP-29 containing benzene groups has some positive effects on the electro-chemical performances. The results confirm that IEP-29-b (equimolar Ptz : benzene; S_{BET} = 586 m^2 g^{-1}) exhibits the fastest redox kinetics, the highest capacitive contribution, and superior rate capability, followed by IEP-29-b/2 (2 : 1 Ptz : benzene ratio; S_{BET} = 559 m^2 g^{-1}), IEP-29-b/4 (4 : 1 Ptz : benzene ratio; S_{BET} = 254 m^2 g^{-1}), and IEP-29 (no benzene; S_{BET} = 29 m^2 g^{-1}). This performance trend is attributed to more efficient charge transfer (lower R_{ct} and E_a, R_{ct}) and improved anion diffusivity (higher D_{anion} and lower E_a, D_{anion}).

3.2.3 Effect of different mass loadings on the performances of electrodes in Li-cells. It is important to note that a majority of research on organic batteries, particularly those employing p-type cathode materials, continues to rely on relatively low mass loadings, typically below 3 mg cm^{-2}. While this conservative strategy helps achieve more favorable electro-chemical parameters, it inherently restricts the achievable areal capacity, often limiting it to values below 1 mA h cm^{-2}. This limitation significantly hinders the practical applicability of such systems. To overcome this, we revisited our earlier success with the buckypaper strategy – a method that enables thick, binder-free electrode fabrication, rather than relying on tradi-tional slurry casting.[62] This method was employed to produce high-mass-loading electrodes from the IEP-29 series that were characterized electrochemically. IEP-29 served as our reference material, with IEP-29-b/4 (a slightly more cross-linked variant) and IEP-29-b (the most cross-linked version) included for comparison. We systematically increased the active mass loading from 2.5 to 50 mg cm^{-2}, all while keeping a high polymer content of 90 wt%.

As shown in Fig. 5, these thick electrodes delivered prom-ising performance in Li-cells at 0.5C. Notably, the IEP-29-b electrode demonstrated commendable tolerance to increased mass loading, exhibiting only a moderate reduction in gravimetric capacity and a slight increase in polarization relative to IEP-29 (Fig. 5a). While gravimetric capacity provides valuable insights into the intrinsic utilization efficiency of the active material, it is the areal capacity that serves as a more relevant metric for evaluating practical applicability, particu-larly in the context of high-energy-demand technologies.[27] Encouragingly, as illustrated in Fig. 5b, areal capacity increased steadily with mass loading across all samples – highlighting the potential of this approach for scalable organic battery technologies.

Fig. 5c illustrates the evolution of both gravimetric and areal capacities as functions of areal mass loading at low C rates (0.5C). Ideally, areal capacity should increase linearly with mass loading; however, in practice, charge transport limitations typically induce nonlinear behavior, particularly at elevated loadings or high current densities.[63] Remarkably, IEP-29-b exhibits nearly linear scaling of areal capacity up to the highest tested loading of 50 mg cm^{-2}, attributed to its efficient mass utilization and retention of near-theoretical gravimetric capacities. In contrast, IEP-29 and IEP-29-b/4 display noticeable deviations from linearity beyond 10 mg cm^{-2} and 20 mg cm^{-2}, respectively. At 50 mg cm^{-2}, capacity utilization declines by 38% for IEP-29 and 27% for IEP-29-b/4, compared to only a 1% reduction for IEP-29-b. These differences translate into areal capacity enhancements of 16-fold for IEP-29, 17-fold for IEP-29-b/4, and 18-fold for IEP-29-b, relative to their respective performances at 2.5 mg cm^{-2}. The absence of a noticeable decrease in gravimetric capacity for IEP-29-b over the tested mass-loading range suggests the potential for further mass loading increases without compromising areal capacity.

In addition to the capacity evaluation at 0.5C, rate capability assessments were conducted across electrodes with varying mass loadings (Fig. 6). Fig. 6a presents the dependence of gravimetric capacity on the C-rate, while the corresponding GCD profiles (Fig. S36–S38) and extended data (Fig. S39 and S40) are provided in the SI. As expected, both gravimetric capacity and rate performance declined with increasing C-rate and polymer mass loading. This decline was particularly

35250 | J. Mater. Chem. A, 2025, **13**, 35242–35256

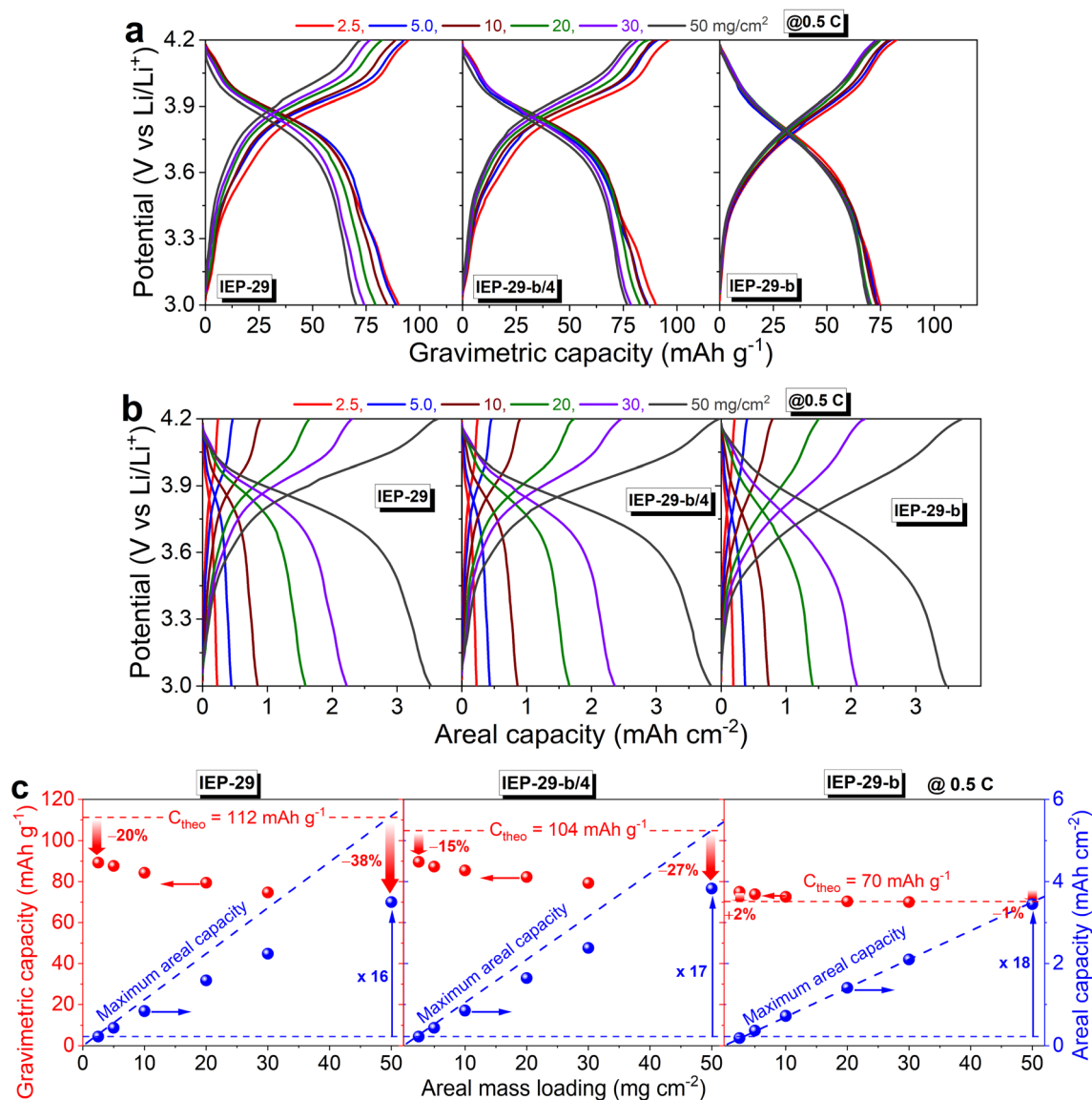This journal is © The Royal Society of Chemistry 2025

Fig. 5 Gravimetric and areal performance evaluation of IEP-29, IEP-29-b/4, and IEP-29-b electrodes with 90 wt% polymer in the electrode having different mass loadings in Li-cells: (a) GCD gravimetric capacity–potential profiles, (b) areal capacity–potential profiles, and (c) the corresponding gravimetric/areal capacities as a function of mass loading at 0.5C.

pronounced in electrodes with the highest loading (50 mg cm^{-2}), especially at C-rates above 2C. Notably, this effect was more significant in IEP-29 electrodes, which exhibited a more significant drop in capacity compared to the more cross-linked than IEP-29-b analogue. For instance, at 10C, IEP-29 electrodes with mass loadings of 2.5, 20, and 50 mg cm^{-2} delivered gravimetric capacities of 57, 14, and 0 mA h g^{-1} (Fig. 6a), corresponding to 64%, 18%, and 0% of their respective capacities at 0.5C (Fig. S41). In contrast, IEP-29-b retained much better rate performance under the same conditions, delivering 47, 32, and 11 mA h g^{-1} (Fig. 6a), equivalent to 63%, 47%, and 15% of their initial 0.5C capacities (Fig. S41). Consistent with the broader electrochemical trends observed across the IEP-29 series, the rate capability followed the order IEP-29-b > IEP-29-b/4 > IEP-29. This hierarchy is attributed to enhanced interaction features due to the more accessible interfaces (i.e. higher

accessible surface areas/porosity) of the further crosslinked variants, which facilitated improved capacity utilization (Fig. S41), reduced potential polarization (Fig. S36–S38), and higher voltage efficiency (Fig. S42).

Furthermore, upon reverting the C-rate back to 0.5C after high-rate cycling, all electrode configurations exhibited near-complete recovery of their original capacities (Fig. S39), highlighting their impressive resilience to rate-induced stress. Capacity retention remained stable over 45 cycles across all mass loadings, underscoring the robust electrochemical reversibility of the systems under demanding conditions. Extending the cycling to 500 cycles at 2C with high-loading electrodes (50 mg cm^{-2}) further demonstrated the superior long-term stability of the IEP-29-b series (Fig. S43). Remarkably, IEP-29-b and IEP-29-b/4 retained 71% and 67% of their initial capacities, respectively, while maintaining high average
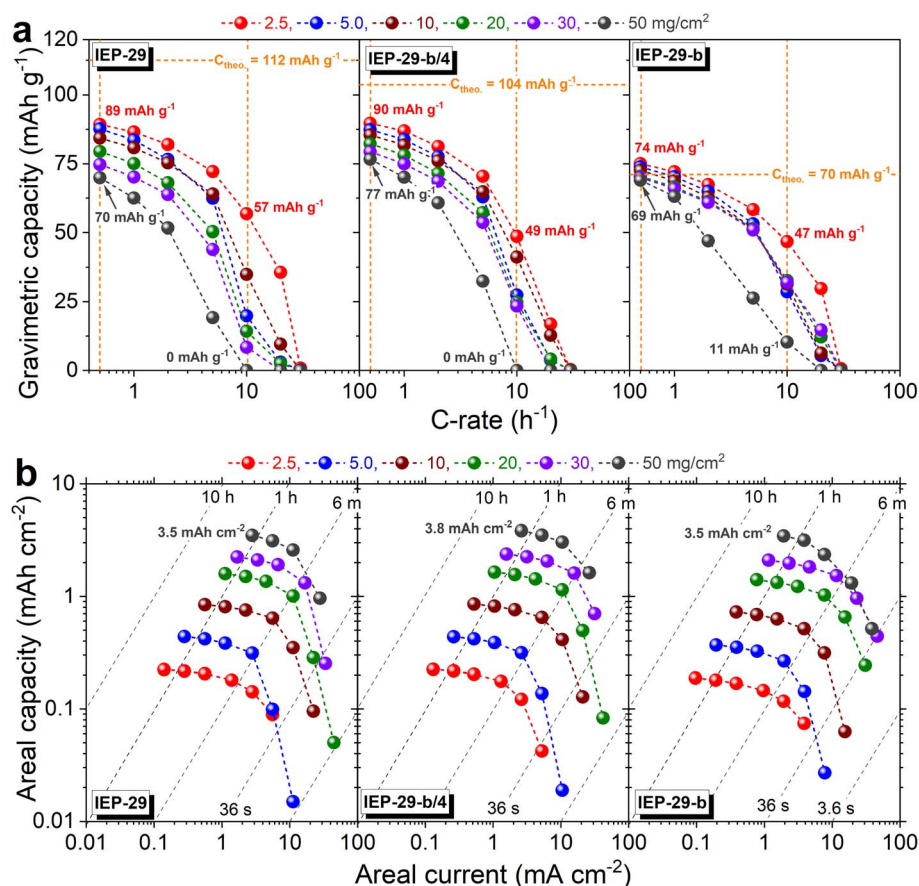
This journal is © The Royal Society of Chemistry 2025

J. Mater. Chem. A, 2025, 13, 35242–35256 | 35251

Fig. 6 Rate performance of IEP-29, IEP-29-b/4, and IEP-29-b electrodes with 90 wt% polymer in the electrode having different mass loadings in Li-cells: (a) gravimetric capacities as a function of C-rate. (b) Areal capacities as a function of areal current.

coulombic efficiencies of 98.9% and 98.4% (Fig. S43 and S44). In contrast, IEP-29 showed significantly poorer cycle stability, retaining only 38% of its capacity and a lower average coulombic efficiency of 97.6%, underscoring the advantages of the more structurally optimized IEP-29 analogues.

As previously mentioned, in terms of areal performance, the high-mass-loading electrodes (50 mg cm^{-2}) of IEP-29, IEP-29-b/4, and IEP-29-b delivered the maximum areal capacities of 3.5, 3.8, and 3.5 mA h cm^{-2}, respectively, at their lowest areal current densities (Fig. 6b). Notably, these electrodes retained substantial areal capacities even at a high C-rate of 5C – 0.96, 1.62, and 1.32 mA h cm^{-2} for IEP-29, IEP-29-b/4, and IEP-29-b, corresponding to current densities as high as 28, 26, and 19.3 mA cm^{-2}, respectively. These results demonstrate the capability of the surface-enhanced variants to deliver high areal capacities under both low and high-rate conditions, making them more suitable for practical energy storage applications.

3.2.4 Comparison of the IEP-29 series with the state-of-the-art p-type cathodes. We benchmarked the electrochemical performance of the IEP-29 series electrodes against the best-performing p-type organic polymer cathodes, including TEMPO- and phenothiazine-based systems, in Li-cells. Fig. 7a presents a comparative analysis of gravimetric capacities, normalized either by using active material mass (commonly reported in the literature) or by using total electrode mass,

which includes all passive components (binders, conductive additives, and current collectors) a parameter more reflective of real-world device performance. The same figure also includes the active material content (%) for each example, offering valuable insight into the compositional efficiency and practical viability of the reported systems. The comparison reveals that while several systems (*e.g.*, PPTZ [entry 4], p-BrPhPT [entry 11], p-DPPZ [entry 13], and TzPz [entry 15], Table S5) exhibit high gravimetric capacities when normalized by using active material mass often exceeding 150 mA h g^{-1}, these values decrease sharply when normalized by using total electrode mass (Fig. 7a). This drop is primarily due to the high proportion of inactive components required to fabricate traditional composite electrodes and the use of a metallic current collector.

By adopting a metal-free buckypaper electrode architecture, we minimized the use of passive materials and achieved a polymer content of 90 wt%, which enabled IEP-29 to attain a gravimetric capacity of 79.2 mA h g^{-1} at the electrode level – being the highest reported so far (for a p-type polymer). In contrast, conventional polymer electrodes with standard active material contents often experience a 20–40% reduction (or even higher 30–90% reduction if we consider the current collector) in electrode-level capacity, compared to just a 10% reduction in our system. Furthermore, we successfully pushed the polymer mass loading to 50 mg cm^{-2} – surpassing typical values in the

35252 | *J. Mater. Chem. A*, 2025, **13**, 35242–35256

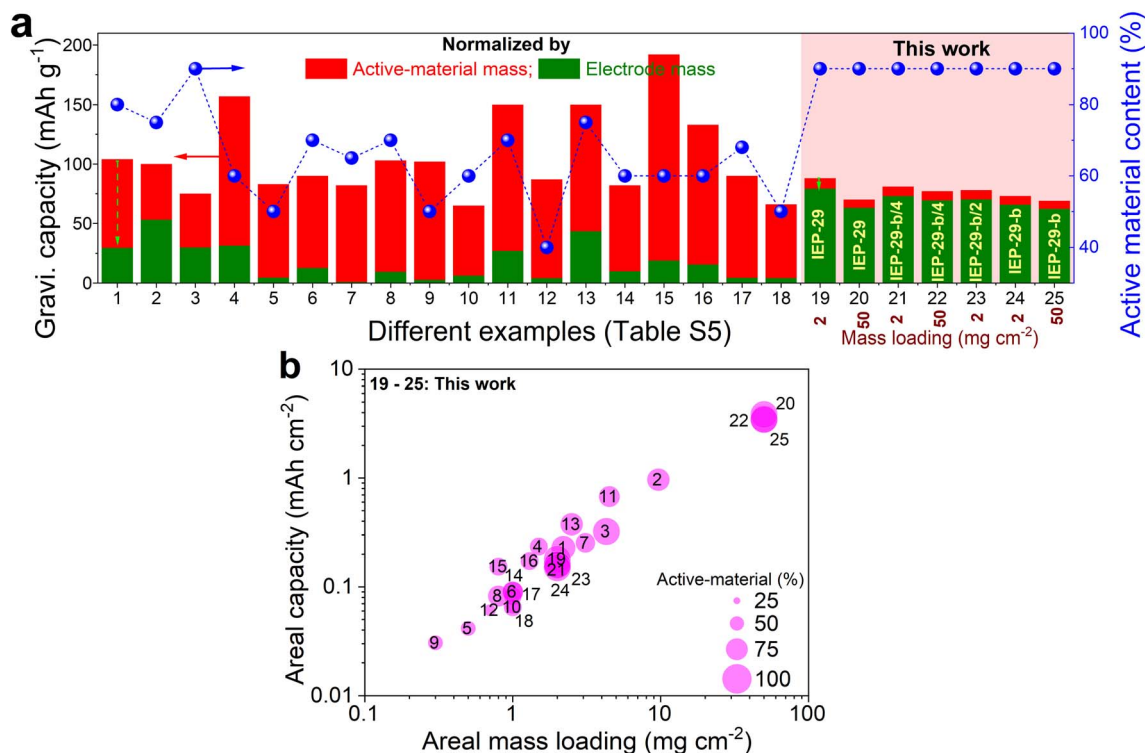This journal is © The Royal Society of Chemistry 2025

Fig. 7 Comparing the electrochemical performance of the IEP-29 series developed in this work with the state-of-the-art p-type cathodes (see Table S5 for the examples) in Li-cells: (a) gravimetric capacity (based on active-material mass – red bars and total mass of electrode – green bars) and active-material content (blue dots). (b) Areal capacity and areal mass loading. These plots for various active-materials are computed by considering some of the best-performing p-type organic electrodes in Li-cells (see Table S5). These active-materials are: PTVE (entry 1),[64] PTMA (entry 2),[65] PTh (entry 3),[66] PPTZ (entry 4),[35] PPTZPZ (entry 5),[67] HPPT (entry 6),[34] poly3a (entry 7),[68] X-PVMPT (entry 8),[57] PVMPT (entry 9),[58] P1b (entry 10),[59] p-BrPhPT (entry 11),[69] POEP; X=O (entry 12),[70] p-DPPZ (entry 13),[71] DAPO−TpOMe-COF (entry 14),[72] TzPz (entry 15),[73] P3 (entry 16),[74] p-DPICZ-O (entry 17),[75] P1 (entry 18)[76] and, the IEP-29 series (this work; entries 19–25).

field. As a result, IEP-29-b/4 demonstrated an areal capacity of 3.8 mA h cm^{-2}, which, to the best of our knowledge, is the highest reported for p-type polymer cathodes in Li-cells (Fig. 7b).

Beyond showcasing excellent performance, this work highlights the importance of reporting gravimetric capacity using both normalization methods. While normalization to active material mass is essential for assessing intrinsic material properties, normalization to total electrode mass offers a more realistic measure of practical performance. Furthermore, reporting areal capacities is crucial for evaluating real-world application potential. The high active material content and elevated mass loading achieved here translate directly into higher energy density and lower projected device costs, highlighting a well-balanced compromise between performance and scalability. Furthermore, for applications such as EVs and portable electronics, where cost and space constraints are critical, electrolyte usage and volumetric energy density should also be considered – factors that have yet to be systematically studied in the context of porous organic electrodes.

4. Conclusion

A series of p-type hypercrosslinked PTz-based OEMs bearing different accessible surface areas were synthesized by using knitting polymerization. The surface morphology observed by SEM measurements indicated more free voids, and the accessible surface areas calculated *via* the BET method became higher on increasing the added amount of the co-monomer, benzene. The detected S_{BET} values were 29, 254, 559, and 586 m^2 g^{-1} for IEP-29, IEP-29-b/4, IEP-29-b/2, and IEP-29-b, respectively. Spectral characterization studies such as ^{13}C CP-MAS NMR and FT-IR revealed the expected systematic changes along the structure. Particularly, an increase in the intensity of the peak at around 130 ppm and the reduction of the resonances at 113 ppm were monitored by ^{13}C CP-MAS NMR, which should be coming from the aromatic carbons neighboring methylene bridges and PTz carbons, respectively. Moreover, CHNS elemental analysis results showed the lower number of heteroatoms on increasing the benzene content since they are only present on the PTz moieties. Indeed, the measurement also allowed us to predict the theoretical gravimetric capacities by taking N% as the reference, as it is the redox active site of the PTz building block. The buckypaper electrodes of the IEP-29 series were evaluated at a standard mass loading of 2.0 mg cm^{-2} across varying polymer contents (50–90 wt%), and exhibited a consistent performance trend, IEP-29-b > IEP-29-b/2 > IEP-29-b/4 > IEP-29 for capacity utilization and rate capability. IEP-29-b demonstrated full capacity utilization (73 mA h g^{-1} at 0.5C; 42 mA h g^{-1} at 10C) and 58%

This journal is © The Royal Society of Chemistry 2025

J. Mater. Chem. A, 2025, **13**, 35242–35256 | **35253**

retention at high rates, supported by EIS, GITT, and CV analyses, indicating superior redox kinetics and ion transport. At a fixed polymer content (90 wt%), increasing the electrode mass loading up to 50 mg cm^{-2} preserved this trend, with IEP-29-b achieving linear areal capacity scaling (3.45 mA h cm^{-2} at 50 mg cm^{-2}). As expected, the trend for specific capacities followed the opposite pattern, highlighting a key trade-off in electrode design: while the more crosslinked variants, such as IEP-29-b, excel in material utilization, rate performance, and long-term stability, the less crosslinked forms offer superior gravimetric capacity. Notably, IEP-29-b/4 exhibited an excellent balance between specific gravimetric and areal capacities, achieving record values of 72.9 mA h g^{-1} (based on the total electrode mass) and 3.85 mA h cm^{-2}, respectively – among the highest reported for p-type polymer cathodes in Li cells. This impressive performance underscores the potential of this variant for high-capacity, scalable energy storage systems. Furthermore, the use of commercially available, low-cost precursors and a one-step synthesis further highlights the practical scalability of this platform. Overall, this study establishes a clear structure–property–performance correlation and presents a viable path toward high-performance, scalable organic cathodes for lithium batteries.

Author contributions

Hakan Bildirir: conceptualization; investigation; data curation; formal analysis; methodology; validation; visualization; writing – original draft; writing – review & editing. Nagaraj Patil: conceptualization; data curation; investigation; formal analysis; methodology; validation; visualization; funding acquisition; writing – original draft; writing – review & editing. Sergio Pinilla: formal analysis; methodology; validation; writing – review & editing. Marta Liras: conceptualization; funding acquisition; project administration; resources; supervision; writing – review & editing. Rebeca Marcilla: conceptualization; funding acquisition; project administration; resources; supervision; writing – review & editing.

Conflicts of interest

The authors declare that they have no known competing financial interests or personal relationships that could have appeared to influence the work reported in this paper.

Data availability

Data are available upon request from the authors.

Supplementary information is available. See DOI: **https://doi.org/10.1039/d5ta04431f**.

Acknowledgements

References

1 I. Overland, J. Juraev and R. Vakulchuk, *Renewable Energy*, 2022, **200**, 379–386.

2 F. Herrmann and F. Rothfuss, in *Advances in Battery Technologies for Electric Vehicles*, ed. B. Scrosati, J. Garche, and E. V. Tillmetz, Woodhead Publishing, 2015, pp. 3–16.

3 Y. Yang, S. Bremner, C. Menictas and M. Kay, *Renew. Sustain. Energy Rev.*, 2018, **91**, 109–125.

4 M. Kolodziejski and I. Michalska-Pozoga, *Energies*, 2023, **16**, 1122.

5 K. L. Hund, D. L. P. Arrobas, F. Masllovet, T. Phuong, T. J. Laing and J. R. Drexhage, *Minerals for Climate Action: The Mineral Intensity of the Clean Energy Transition (English)*, World Bank, Washington, D.C., 2023.

6 S. Dühnen, J. Betz, M. Kolek, R. Schmuch, M. Winter and T. Placke, *Small Methods*, 2020, **4**, 2000039.

7 J. Kim, Y. Kim, J. Yoo, G. Kwon, Y. Ko and K. Kang, *Nat. Rev. Mater.*, 2023, **8**, 54–70.

8 J. Bitenc, K. Pirnat, O. Lužanin and R. Dominko, *Chem. Mater.*, 2024, **36**, 1025–1040.

9 R. Shi, S. Jiao, Q. Yue, G. Gu, K. Zhang and Y. Zhao, *Exploration*, 2022, **2**, 220066.

10 Y. Liang and Y. Yao, *Joule*, 2018, **2**, 1690–1706.

11 R. Dantas, C. Ribeiro and M. Souto, *Chem. Commun.*, 2024, **60**, 138–149.

12 N. Goujon, N. Casado, N. Patil, R. Marcilla and D. Mecerreyes, *Prog. Polym. Sci.*, 2021, **122**, 101449.

13 Y. Lu, Y. Cai, Q. Zhang and J. Chen, *Adv. Mater.*, 2022, **34**, 2104150.

14 H. Dong, N. Kang, L. Li, L. Li, Y. Yu and S. Chou, *Adv. Mater.*, 2024, **36**, 2311401.

15 P. Rohland, E. Schröter, O. Nolte, G. R. Newkome, M. D. Hager and U. S. Schubert, *Prog. Polym. Sci.*, 2022, **125**, 101474.

16 K. Oyaizu and H. Nishide, *Adv. Mater.*, 2009, **21**, 2339–2344.

17 M. E. Bhosale, S. Chae, J. M. Kim and J.-Y. Choi, *J. Mater. Chem. A*, 2018, **6**, 19885–19911.

18 H. Wang, C.-J. Yao, H.-J. Nie, K.-Z. Wang, Y.-W. Zhong, P. Chen, S. Mei and Q. Zhang, *J. Mater. Chem. A*, 2020, **8**, 11906–11922.

19 X. Liu, C.-F. Liu, W.-Y. Lai and W. Huang, *Adv. Mater. Technol.*, 2020, **5**, 2000154.

20 S. Suleman, X. Cheng, M. Gu and Y. Kim, *Commun. Mater.*, 2025, **6**, 78.

21 R. Wessling, P. Penert and B. Esser, *Adv. Energy Mater.*, 2025, **15**, 2500150.

22 Y. Qi, H. Zhao, L. Chen and Y. Lei, *Small*, 2025, 2412769.

23 G. Berckmans, M. Messagie, J. Smekens, N. Omar, L. Vanhaverbeke and J. Van Mierlo, *Energies*, 2017, **10**, 1314.

35254 | *J. Mater. Chem. A*, 2025, **13**, 35242–35256

This journal is © The Royal Society of Chemistry 2025

24 R. Schmuch, R. Wagner, G. Hörpel, T. Placke and M. Winter, *Nat. Energy*, 2018, **3**, 267–278.

25 J. Xiao, Y. Huang, Y. Ma, C. Li, L. Fu, W. Zeng, X. Wang, X. Li, M. Wang, B. Guo, Y. Lin and H. Cao, *Energy Storage Mater.*, 2023, **63**, 103046.

26 H. Kye, Y. Kang, D. Jang, J. E. Kwon and B. G. Kim, *Adv. Energy Sustain. Res.*, 2022, **3**, 202200030.

27 F. Wu, M. Liu, Y. Li, X. Feng, K. Zhang, Y. Bai, X. Wang and C. Wu, *Electrochem. Energy Rev.*, 2021, **4**, 382–446.

28 A. Palma-Cando and U. Scherf, *ACS Appl. Mater. Interfaces*, 2015, **7**, 11127–11133.

29 C. Gu, N. Hosono, J.-J. Zheng, Y. Sato, S. Kusaka, S. Sakaki and S. Kitagawa, *Science*, 2019, **363**, 387–391.

30 W. Wang, H. Wang, X. Tang, J. Huo, Y. Su, C. Lu, Y. Zhang, H. Xu and C. Gu, *Chem. Sci.*, 2022, **13**, 8679–8685.

31 S. H. Jiang, X. J. Zhang, Z. C. Zhou, X. Li and T. Cai, *Macromolecules*, 2024, **57**, 9889–9899.

32 C. Yan, Y. Wu, H. Lu, H. Liu, G. Yi, M. Li, X. Cai, S. Gao and Z. Yang, *Microporous Mesoporous Mater.*, 2022, **343**, 112157.

33 B. M. Peterson, D. Ren, L. Shen, Y. C. M. Wu, B. Ulgut, G. W. Coates, H. D. Abruna and B. P. Fors, *ACS Appl. Energy Mater.*, 2018, **1**, 3560–3564.

34 Y. Zhang, P. Gao, X. Guo, H. Chen, R. Zhang, Y. Du, B. Wang and H. Yang, *RSC Adv.*, 2020, **10**, 16732–16736.

35 X. Wang, G. Li, Y. Han, F. Wang, J. Chu, T. Cai, B. Wang and Z. Song, *ChemSusChem*, 2021, **14**, 3174–3181.

36 S. Lv, Q. He, Y. Zhang, J. Guo, X. Peng, Y. Du and H. Yang, *New J. Chem.*, 2023, **47**, 10911–10915.

37 B. Esser, I. H. Morhenn and M. Keis, *Acc. Mater. Res.*, 2025, **6**, 754–764.

38 H. Bildirir, D. Alván, N. Patil, V. A. de la Peña O'Shea, M. Liras and R. Marcilla, *ACS Appl. Polym. Mater.*, 2024, **6**, 10092–10101.

39 A. Fombona-Pascual, N. Patil, E. García-Quismondo, N. Goujon, D. Mecerreyes, R. Marcilla, J. Palma and J. J. Lado, *Chem. Eng. J.*, 2023, **461**, 142001.

40 L. Tan and B. Tan, *Chem. Soc. Rev.*, 2017, **46**, 3322–3356.

41 Z. Liu, T. Yang, Y. Song, N. Zhao, S. Wu, Z. Ma, X. Gong, X. Tian and Z. Liu, *RSC Appl. Polym.*, 2025, **3**, 746–766.

42 R. Dawson, T. Ratvijitvech, M. Corker, A. Laybourn, Y. Z. Khimyak, A. I. Cooper and D. J. Adams, *Polym. Chem.*, 2012, **3**, 2034–2038.

43 S. Dadashi-Silab, H. Bildirir, R. Dawson, A. Thomas and Y. Yagci, *Macromolecules*, 2014, **47**, 4607–4614.

44 R. A. Al-Qahtani, M. M. Abdelnaby, I. Abdulazeez and O. C. S. Al-Hamouz, *Carbon Capture Sci. Technol.*, 2024, **13**, 100330.

45 S. Hou, S. Jin and B. Tan, *Sep. Purif. Technol.*, 2025, **363**, 132168.

46 N. Chaoui, M. Trunk, R. Dawson, J. Schmidt and A. Thomas, *Chem. Soc. Rev.*, 2017, **46**, 3302–3321.

47 A. Laybourn, R. Dawson, R. Clowes, T. Hasell, A. I. Cooper, Y. Z. Khimyak and D. J. Adams, *Polym. Chem.*, 2014, **5**, 6325–6333.

48 M. Thommes, K. Kaneko, A. V. Neimark, J. P. Olivier, F. Rodriguez-Reinoso, J. Rouquerol and K. S. W. Sing, *Pure Appl. Chem.*, 2015, **87**, 1051–1069.

49 B. Li, R. Gong, W. Wang, X. Huang, W. Zhang, H. Li, C. Hu and B. Tan, *Macromolecules*, 2011, **44**, 2410–2414.

50 R. T. Woodward, L. A. Stevens, R. Dawson, M. Vijayaraghavan, T. Hasell, I. P. Silverwood, A. V. Ewing, T. Ratvijitvech, J. D. Exley, S. Y. Chong, F. Blanc, D. J. Adams, S. G. Kazarian, C. E. Snape, T. C. Drage and A. I. Cooper, *J. Am. Chem. Soc.*, 2014, **136**, 9028–9035.

51 G. Kupgan, T. P. Liyana-Arachchi and C. M. Colina, *Langmuir*, 2017, **33**, 11138–11145.

52 B. Li, R. Gong, Y. Luo and B. Tan, *Soft Matter*, 2011, **7**, 10910–10916.

53 J. Coates, in *Encyclopedia of Analytical Chemistry*, 2006.

54 G. Liu, Y. Wang, C. Shen, Z. Ju and D. Yuan, *J. Mater. Chem. A*, 2015, **3**, 3051–3058.

55 H. Bildirir, M. García-Tecedor, M. Gomez-Mendoza, D. Alván, R. Marcilla, V. A. de la Peña O'Shea and M. Liras, *Small*, 2024, **20**, 2404120.

56 N. Patil, J. I. Medina-Santos, E. García-Quismondo, N. Goujon, D. Mecerreyes, J. Palma and R. Marcilla, *Energy Storage Mater.*, 2025, **78**, 104254.

57 F. Otteny, M. Kolek, J. Becking, M. Winter, P. Bieker and B. Esser, *Adv. Energy Mater.*, 2018, **8**, 1802151.

58 V. Perner, D. Diddens, F. Otteny, V. Küpers, P. Bieker, B. Esser, M. Winter and M. Kolek, *ACS Appl. Mater. Interfaces*, 2021, **13**, 12442–12453.

59 P. Acker, L. Rzesny, C. F. N. Marchiori, C. M. Araujo and B. Esser, *Adv. Funct. Mater.*, 2019, **29**, 1906436.

60 V. Augustyn, J. Come, M. A. Lowe, J. W. Kim, P.-L. Taberna, S. H. Tolbert, H. D. Abruña, P. Simon and B. Dunn, *Nat. Mater.*, 2013, **12**, 518–522.

61 T. Brezesinski, J. Wang, S. H. Tolbert and B. Dunn, *Nat. Mater.*, 2010, **92**(9), 146–151.

62 A. Molina, N. Patil, E. Ventosa, M. Liras, J. Palma and R. Marcilla, *ACS Energy Lett.*, 2020, **5**, 2945–2953.

63 Y. Zhang, Y. Shi, X.-C. Hu, W.-P. Wang, R. Wen, S. Xin and Y.-G. Guo, *Adv. Energy Mater.*, 2020, **10**, 1903325.

64 M. Suguro, S. Iwasa and K. Nakahara, *Macromol. Rapid Commun.*, 2008, **29**, 1635–1639.

65 A. Innocenti, I. Á. Moisés, O. Lužanin, J. Bitenc, J.-F. Gohy and S. Passerini, *ACS Appl. Mater. Interfaces*, 2024, **16**, 48757–48770.

66 P. Acker, J. S. Wössner, G. Desmaizieres and B. Esser, *ACS Sustain. Chem. Eng.*, 2022, **10**, 3236–3244.

67 F. A. Obrezkov, A. I. Somova, E. S. Fedina, S. G. Vasil'ev, K. J. Stevenson and P. A. Troshin, *Energy Technol.*, 2021, **9**, 2000772.

68 T. Godet-Bar, J. C. Leprêtre, O. Le Bacq, J. Y. Sanchez, A. Deronzier and A. Pasturel, *Phys. Chem. Chem. Phys.*, 2015, **17**, 25283–25296.

69 J. Lv, J. Ye, G. Dai, Z. Niu, Y. Sun, X. Zhang and Y. Zhao, *J. Energy Chem.*, 2020, **47**, 256–262.

70 X. Zhang, Q. Xu, S. Wang, Y. Tang and X. Huang, *ACS Appl. Energy Mater.*, 2021, **4**, 11787–11792.

71 G. Dai, X. Wang, Y. Qian, Z. Niu, X. Zhu, J. Ye, Y. Zhao and X. Zhang, *Energy Storage Mater.*, 2019, **16**, 236–242.

This journal is © The Royal Society of Chemistry 2025

J. Mater. Chem. A, 2025, **13**, 35242–35256 | **35255**
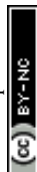
72 Z. Meng, Y. Zhang, M. Dong, Y. Zhang, F. Cui, T.-P. Loh, Y. Jin, W. Zhang, H. Yang and Y. Du, *J. Mater. Chem. A*, 2021, **9**, 10661–10665.

73 W. Ma, L.-W. Luo, P. Dong, P. Zheng, X. Huang, C. Zhang, J.-X. Jiang and Y. Cao, *Adv. Funct. Mater.*, 2021, **31**, 2105027.

74 P. Acker, M. E. Speer, J. S. Wössner and B. Esser, *J. Mater. Chem. A*, 2020, **8**, 11195–11201.

75 G. Dai, Y. Gao, Z. Niu, P. He, X. Zhang, Y. Zhao and H. Zhou, *ChemSusChem*, 2020, **13**, 2264–2270.

76 M. E. Speer, M. Kolek, J. J. Jassoy, J. Heine, M. Winter, P. M. Bieker and B. Esser, *Chem. Commun.*, 2015, **51**, 15261–15264.

35256 | *J. Mater. Chem. A*, 2025, **13**, 35242–35256

This journal is © The Royal Society of Chemistry 2025